Journal of Chromatography A, 1217 (2010) 394–404

Contents lists available at ScienceDirect

Journal of Chromatography A

journal homepage: www.elsevier.com/locate/chroma

Numerical solutions for isoelectric focusing and isotachophoresis problems

Ying Chou, Ruey-Jen Yang*

Department of Engineering Science, National Cheng Kung University, 1 University Rd, Tainan, Taiwan

ARTICLE INFO

Article history:
Received 24 September 2009
Received in revised form 9 November 2009
Accepted 16 November 2009
Available online 3 December 2009

Keywords:
Isoelectric focusing (IEF)
Isotachophoresis (ITP)
Adaptive mesh redistribution (AMR)
CESE method

ABSTRACT

This study combines an adaptive mesh redistribution (AMR) method and the space–time conservation element and solution element (CESE) method to construct a high-resolution scheme for the solution of electrophoresis pre-concentration and separation problems. In the proposed AMR–CESE scheme, the fine mesh points are moved toward the regions of discontinuity within the solution domain in accordance with the equidistribution principle. To reduce the numerical dissipation within the regions of the solution domain with a large spatial mesh, the spatial component of the CESE scheme is treated using a Courant–Friedrichs–Lewy (CFL) number insensitive scheme. The validity of the proposed approach is confirmed by comparing the results obtained for typical isoelectric focusing (IEF) and isotachophoresis (ITP) problems with those obtained from the conventional CESE scheme and the finite volume method (FVM), respectively. It is shown that the AMR–CESE scheme yields a better accuracy than uniform fixed-mesh solvers with no more than a minor increase in the computational cost.

1. Introduction

Electrophoretic separation encompasses a variety of well-established techniques for fractionating mixtures of ionic solutes for analytical and preparative applications. Due to the miniature scale of electrophoretic systems, numerical simulations have emerged as the method of choice for obtaining detailed insights into the roles of electro-migration and diffusion in accomplishing a variety of electrophoresis phenomena, including capillary zone electrophoresis (CZE), isotachophoresis (ITP) and isoelectric focusing (IEF). However, traditional numerical methods have several disadvantages when applied to the analysis of electrophoresis problems, including numerical oscillation, dispersion and dissipation. Accordingly, this study presents an enhanced performance numerical method in which the space–time conservation element and solution element (CESE) method is integrated with an adaptive mesh redistribution (AMR) scheme. The feasibility of the proposed AMR–CESE scheme is demonstrated by comparing the simulation results obtained for various ITP and IEF problems with those obtained from existing numerical techniques such as the original CESE method and the finite volume method (FVM), respectively.

In the ITP process, the sample is injected between two electrolytes, one containing a co-ion with a high mobility and the other containing a slower co-ion with a mobility which is lower than the mobility of the sample ions. During the separation process, the analytes gradually separate into distinct zones under the effects of an externally applied electric field. In the steady-state condition, these zones are arranged in order of their respective mobilities and migrate with the same velocity. An excellent historical overview of the ITP process is presented by Righetti [1], while more recent developments in the field are described by Gebauer et al. [2]. Křivánková et al. [3] presented a comprehensive analysis of the ITP problem in zone electrophoresis applications with particular emphasis on the effects of transient ITP mechanisms on the migration time and separation efficiency, respectively. Shim et al. [4] utilized a simulation technique to investigate the problems of ITP stacking and induced pH-junction focusing, respectively. In general, the results demonstrated the dual stacking mechanism based on transient ITP and induced pH-junction focusing as a means to increase the concentration sensitivity in capillary electrophoresis. In recent years, researchers have demonstrated the potential for exploiting ITP to accomplish a variety of operations in networked microfluidic devices [5]. Various high-resolution simulators have been presented for analyzing electrophoresis separation problems, including SIMUL5, developed by Hruška et al. [6] and available free-of-charge at www.natur.cuni.cz/gas, and the IEF configuration consisting of 100-carrier ampholytes was first simulated by Thormann and Mosher [7]. These simulation schemes suppress numerical oscillations when implemented using a grid with a sufficiently fine mesh. However, the corresponding increase in the computational cost is encountered. Yu et al. [8] utilized the CESE method to model various ITP and zone electrophoresis (ZE) problems and showed that the solutions were more robust than those obtained using traditional forward time central space (FTCS) method and more accurate than those solved by the upwind

* Corresponding author. Tel.: +886 6 2002724; fax: +886 6 2766549.
E-mail address: rjyang@mail.ncku.edu.tw (R.-J. Yang).

0021-9673/$ – see front matter © 2009 Elsevier B.V. All rights reserved.
doi:10.1016/j.chroma.2009.11.044

method. In a recent study, Bercovici et al. [9] developed an open source simulation tool (Spresso, http://microfluidics.stanford.edu) for analyzing pre-concentration and separation effects in CZE and ITP applications. Besides, it was shown that the compact scheme combined with adaptive grid algorithm can reduce much computational time.

Isoelectric focusing (IEF) is a high-resolution electrophoretic technique in which amphoteric biomolecules are separated and concentrated at their isoelectric points (p*I*s) in a pH gradient under the application of an external electric field. IEF is conventionally performed in either an ampholyte solution or an immobilized pH gradient (IPG) gel and has attracted significant attention in recent decades due to its wide applicability in a diverse range of fields, including chemistry, biochemistry and pharmacology. An excellent review of IEF and its technical aspects is presented by Silvertand et al. [10]. Many mathematical models have been proposed for analyzing the IEF problem and other microfluidic phenomena. For example, in 1986, Mosher et al. [11] presented a mathematical model to describe the electrophoretic behavior of proteins within simple microchannel geometries. In a later study, the authors applied the model to simulate transitional protein distributions within a simple buffer mixture under the effects of an external electric field [12]. Sounart and Baygents [13] simulated the electrophoretic separation problem using a transient 1D electrophoresis model and the flux-corrected transport (FCT) finite difference method. Chatterjee [14] presented a generic unified approach for modeling the transport phenomena and chemical behavior of weak, multivalent analytes with multiple physics and driving forces. Hruška et al. [6] used a mathematical model based on the principles of mass conservation, acid–base equilibria and electro-neutrality to construct a freeware program (Simul) designed to simulate the movement of ions in liquid solutions under the effects of an external electric field. Recently, a 2D finite volume model to simulate non-linear IEF in a contraction–expansion channel was developed by Shim et al. [15]. Furthermore, Chou and Yang [16] integrated the conventional CESE method with a CFL number insensitive scheme in order to improve the accuracy of the CESE simulation results obtained for a 1D IEF problem in a contraction–expansion channel. Recently, the review paper by Thormann et al. [17] gives an overview on the dynamic computer simulations of electrophoresis including moving boundary electrophoresis, zone electrophoresis, ITP, IEF and EKC.

Adaptive moving mesh methods are widely used in solving a variety of scientific and engineering problems in which singular or nearly singular solutions are developed dynamically within fairly localized regions of the solution domain. Investigating problems of this type using numerical methods requires the use of extremely fine meshes over a small portion of the physical domain in order to resolve the large solution variations. The successful implementation of an adaptive mesh strategy not only increases the accuracy of the numerical approximations, but also reduces the computational cost by focusing the mesh points in the regions of the solution domain where they are most required, e.g. regions of the solution domain corresponding to shock waves, boundary layers, detonation waves, and so on. The main references of this study follows: Tang and Tang [18] developed an adaptive mesh algorithm comprising two stages, namely a partial differential equation (PDE) evolution stage and a mesh redistribution stage. In executing the solution procedure, the mesh algorithm was designed to ensure the "mass" conservation of the underlying numerical solutions each time the solution domain was remeshed. Huang [19] examined the practical aspects involved in formulating and solving moving mesh partial differential equations (MMPDEs) and described the importance of defining an appropriate monitor function in order to facilitate an explicit control of the mesh concentration. Beckett and Mackenzie [20] had analyzed the convergence properties of various moving mesh methods and concluded that the grid was suggested by the equidistribution of a positive monitor function which is a linear combination of a constant floor and a power of the second derivative of the solution. Jin and Xu [21] and Tang [22] demonstrated the feasibility of utilizing adaptive moving mesh methods to solve a variety of computational fluid dynamics (CFD) problems and other physical problems, including the two-dimensional viscous flows and the solution of the shallow-water equations.

The CESE method was originally developed by Chang [23] in 1995 as a means of solving the Navier–Stokes and Euler equations within the context of CFD and aero-acoustic problems. The overriding principle of the CESE method is to ensure flux conservation at both the local and the global level in the space–time domain. In the CESE method, both the independent flow variables and their derivatives are treated as unknowns and are solved simultaneously. Importantly, there is no need to adjust the artificial dissipation parameters to match the local solution properties, and hence a uniform solution accuracy is assured. These features render the CESE method an ideal solver for problems characterized by discontinuous phenomena or steep gradients, such as combustion systems, shock waves [24], thermal waves [25], and so on. Due to the explicit nature of the CESE solution procedure, the CFL number (i.e. the product of the local velocity and the ratio of the time interval to the grid size) must be less than unity to ensure the stability of the numerical solutions. However, for very small CFL numbers (i.e. CFL < 0.1), the CESE scheme becomes overly dissipative, and hence the solution procedure fails to converge. To resolve this problem, Chang [26] developed a CFL number insensitive (CNI)-CESE scheme, and demonstrated its ability to resolve Sod's shock tube problem for CFL numbers ranging from 1 to less than 0.001. Thus, to prevent the numerical dissipation due to the low CFL number caused some large value of $(\Delta x)_j$ after mesh moving, we established the CFL number insensitive scheme on the non-uniform mesh to accomplish the provided AMR–CESE scheme.

In the current study, the AMR–CESE method is proposed to model the ITP and IEF electrophoretic separation phenomena. The study commences by formulating a general model for capillary electrophoretic separation and then presents a detail description how to combine the CESE scheme and the adaptive mesh method. Detailed solutions are calculated for the ITP and IEF phenomena under a variety of initial and operating conditions. The quality of the AMR–CESE solutions is evaluated via a comparison with the results obtained under equivalent conditions by original CESE scheme and FVM.

2. Mathematical model

This section commences by developing a generalized dissociation model for multivalent analytes. A general model for the transport of ionic and neutral compounds in IEF applications is then derived.

2.1. Generalized dissociation model for multivalent analytes

For a general analyte A with n dissociable protons, a total of n dissociation reactions may take place. (Note that the details of these dissociation reactions and the corresponding parameters are presented in [14] and are therefore omitted here). In general, the degree of dissociation of an ionic state containing j dissociable protons A_i is defined as

$$\alpha_i = \frac{C_i}{C} = \frac{[H^+]^{-(n-i)}\prod_{l=1}^{n-i}K_l}{1+\sum_{j=1}^{n}[H^+]^{-j}\prod_{l=1}^{j}K_l}, \quad i \neq n,$$
$$\alpha_i = \frac{1}{1+\sum_{j=1}^{n}[H^+]^{-i}\prod_{l=1}^{i}K_l}, \quad i = n, \tag{1}$$

where C denotes the overall concentration of analyte A, C_i indicates the concentration of analyte A_i, and K_l is the equilibrium rate constant.

As discussed in [14], the charge and mobility parameters of an analyte can be derived by treating the ensemble of all the states as a single entity governed by effective parameters rather than by treating each ionic state as a separate variable. The effective charge, Z_{eff}, and effective mobility, ω_{eff}, of a multivalent analyte can be expressed, respectively, as

$$Z_{\text{eff}} = \sum_{i=0}^{n} (\nu - i)\alpha_{n-i}, \tag{2}$$

where ν is the net charge of the analyte when possessing all n dissociable protons, and

$$\omega_{\text{eff}} = \frac{1}{Z_{\text{eff}}} \sum_{i=0}^{n} (\nu - i)\omega_i \alpha_i, \tag{3}$$

where ω_i is the mobility of ionic state A_i.

2.2. General transport model

A general set of balance laws governing the transport of ionic and neutral compounds in isothermal electrophoretic separations will be introduced in this section. The basic governing equation for the transport of an ionic compound in an isothermal electrophoretic separation can be formulated in terms of the following mass flux conservation equation:

$$\frac{\partial C}{\partial t} = -\nabla \cdot (\vec{U}C + \vec{V}_{\text{e}}C - D\nabla C), \tag{4}$$

where $\vec{U}$ is the bulk flow velocity; $\vec{V}_{\text{e}}$ is the electrophoretic velocity, i.e. $\vec{V}_{\text{e}} = Z_{\text{eff}}\omega_{\text{eff}}\vec{E}_l$, where $\vec{E}_{\text{l}}$ is the intensity of the local electric field; and D is the diffusion coefficient, i.e. $D = RT\omega_{\text{eff}}/F$ from the Nernst–Einstein equation, where R is the gas constant, T is the absolute temperature and F is the Faraday constant [27]. In deriving a simplified 1D transport model, the EOF (electroosmotic flow) is not accounted. Consequently, electrokinetic flow does not take place [28,29]. In the absence of a bulk flow (such as that induced by an external pressure force, for example), Eq. (4) reduces to

$$\frac{\partial C}{\partial t} = -\frac{\partial}{\partial x}\left(V_{\text{e}}C - D\frac{\partial C}{\partial x}\right). \tag{5}$$

It is well known that hydrogen ions play an essential role in all dissociation reactions which produce or consume protons, e.g. the dissociation of water to create a hydroxyl ion and a hydrogen ion. Furthermore, the pH of a solution can be determined from the net neutrality assumption, i.e.

$$[\text{H}^+] - \frac{K_{\text{W}}}{[\text{H}^+]} + \sum_{i=1}^{N} (Z_{\text{eff}})_i C_i = 0, \tag{6}$$

where $[\text{H}^+]$ is the concentration of the hydrogen ions and K_{W} is the dissociation constant of water. (Note that the actual pH value is obtained by applying the Newton–Raphson method to determine the root of Eq. (6)).

In an electrophoretic separation process, the migration velocity varies as a function of the strength of the local electric field $\vec{E}_{\text{l}}$, which in turn depends on the conductivity σ of the species, i.e.

$$\sigma = F\left[[\text{H}^+]\omega_{\text{H}} + \frac{K_{\text{W}}}{[\text{H}^+]}\omega_{\text{OH}} + \sum_{i=1}^{N} (Z_{\text{eff}}^2)(\omega_{\text{eff}})_i C_i\right], \tag{7}$$

where ω_{H} and ω_{OH} are the mobilities of the hydrogen ions and the hydroxide ions, respectively. According to the modified Ohm's law, the local electric field strength is related to the current density $\vec{I}$ and conductivity σ via the following formulation [6]:

$$\vec{E}_l = \frac{\vec{I}}{\sigma} - \frac{F}{\sigma}\left[-D_{\text{H}}\frac{\partial C_{\text{H}}}{\partial x} + D_{\text{OH}}\frac{\partial C_{\text{OH}}}{\partial x} - \sum_{i=1}^{N} (z_{\text{eff}})_i D_i \frac{\partial C_i}{\partial x}\right], \tag{8}$$

where D_{H} and D_{OH} are the diffusion coefficients of hydrogen and hydroxide ions, respectively. The second term on the right-hand side accounts for the diffusion potential rising due to differential diffusion of dissimilar ionic species of constituents. And thus the migration velocity can be derived as $\vec{V}_{\text{e}} = (\omega_{\text{eff}})\vec{E}_{\text{l}}$.

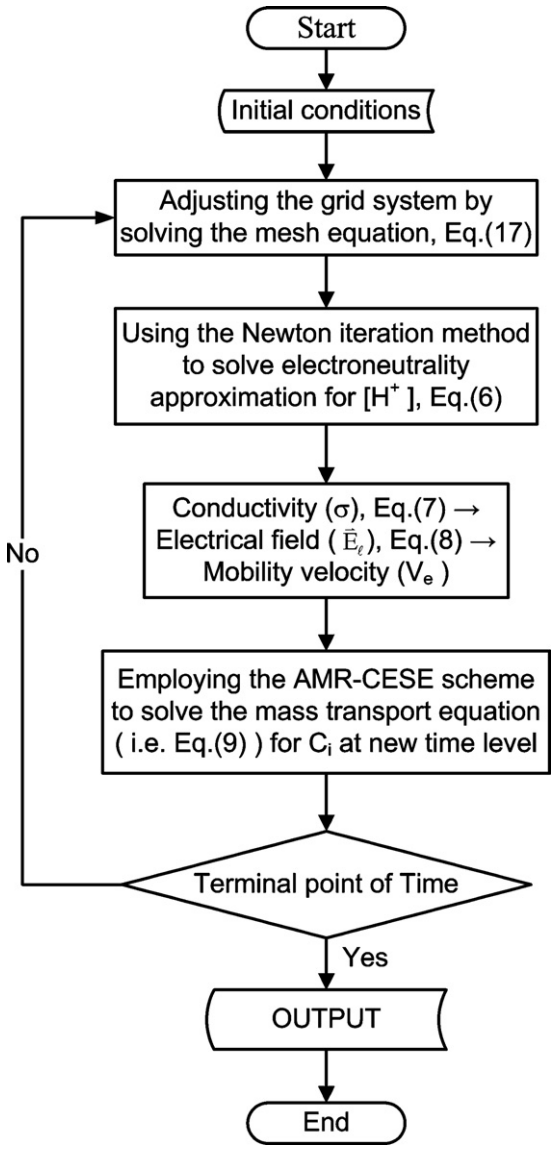

Fig. 1. Flowchart showing the implementation of proposed AMR–CESE scheme.

3. Numerical implementation

As discussed in Section 1, this paper proposes an adaptive mesh redistribution CESE (AMR–CESE) scheme for obtaining high-resolution solutions for electrophoretic separation problems in a computationally efficient manner. Fig. 1 presents a flowchart showing the application of the AMR–CESE scheme to the simplified 1D transport equation described in Section 2.2. As shown, the solution procedure commences by assigning a suitable set of initial

conditions (e.g. the grid size, the distributions of analytes, parameters of each analytes and the value of applied voltage). The grid mesh is then adjusted in such a way as to increase the resolution within the regions of interest within the solution domain by solving the mesh equation (Eq. (18)) and the solution is updated on the new mesh using an appropriate solution-update formulation (Eq. (22)). The Newton–Raphson iteration method is then applied to solve the charge conservation equation given in Eq. (6) in order to determine the $[H^+]$ distribution resulting from the ionic association/dissociation process. Subsequently, Eq. (7) is solved to obtain the local conductivity (σ), which is then integrated over the channel to establish the total resistance. Given a knowledge of the applied voltage, $\vec{E}$, the current density $\vec{I}$ within the channel is then computed in accordance with modified Ohm's law. Thereafter, the local electric field strength and mobility velocity are derived using the Eq. (8), and $\vec{V}_e = (\omega_{eff})\vec{E}_l$, respectively. Having determined the values of all these parameters, the 1D transport equation is solved for the next time step The solution procedure continues iteratively in this way until the specified termination of physical time is achieved satisfied, at which point the solutions for the concentrations, pH profile and conductivity distribution within the channel are obtained.

The following sections review two of the fundamental mechanisms embedded within the proposed AMR–CESE scheme, namely the non-uniform mesh CESE scheme and the CFL number insensitive CESE scheme.

3.1. Non-uniform mesh CESE scheme

In moving mesh methods, the action of moving the grid points to the regions of interest within the solution domain has the effect of producing a non-uniform mesh system. Thus, this section provides a simple method for implementing the CESE algorithm utilizing a non-uniform mesh in such a way that flux conservation is maintained at both the local and the global level.

The 1D IEF transport model for the ith species given in Eq. (5) can be expressed in the following matrix form:

$$\frac{\partial U}{\partial t} + \frac{\partial E}{\partial x} = 0, \tag{9}$$

where $U = C_i$ and $E = (V_{e,i}C_i - D_i(\partial C_i/\partial x))$.

Let $\xi_1 = t$ and $\xi_2 = x$ be the coordinates of a two-dimensional Euclidean space E_2. Applying the Gaussian divergence theorem in E_2, the differential form of Eq. (9) can be transformed into the following integral conservation form:

$$\int_{S(V)} \vec{h} \cdot d\vec{s} = 0, \tag{10}$$

where $\vec{h} = (E, U)$ and $S(V)$ is the boundary of an arbitrary space–time region V in E_2.

As shown in Fig. 2(a), in the CESE scheme, the Euclidean space E_2 is partitioned into a non-uniform array of non-overlapping rectangular regions referred to as conservation elements (CEs). Fig. 2(b) presents a detailed view of an arbitrarily chosen conservation element CE(j, n), in which the midpoint of the upper surface is located at mesh point (j, n). Finally, let the solution element SE (j, n) be the interior of the space–time region bounded by a dashed curve depicted in Fig. 2(c). It includes a horizontal line segment, a vertical segment and their immediate neighborhood. Consequently, the boundary of CE(j, n) is a subset of the union of solution elements (SEs) (j, n), $(j-1/2, n-1/2)$ and $(j+1/2, n-1/2)$, respectively.

For any $(x,t) \in$ SE(j, n), let U, E and $\vec{h}$ be approximated by U^*, E^* and $\vec{h}^*$, respectively, with the following first-order Taylor's expansion

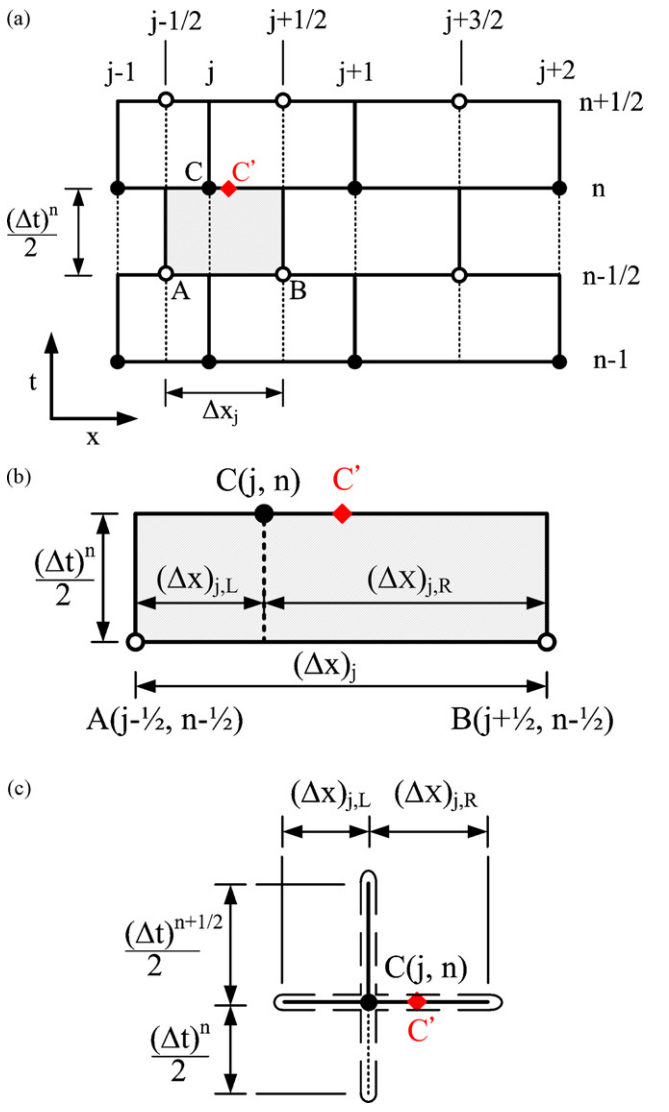

Fig. 2. Discretization of non-uniform AMR–CESE scheme in space–time domain: (a) space–time mesh; (b) conservation element (CE) of node (n, j); (c) solution element (SE) of node (n, j).

forms:

$$\begin{aligned} U^*(x,t;j,n) &= (U)_j^n + (x-x_j)(U_x)_j^n + (t-t^n)(U_t)_j^n, \\ E^*(x,t;j,n) &= (E)_j^n + (x-x_j)(E_x)_j^n + (t-t^n)(E_t)_j^n, \\ \vec{h}^*(x,t;j,n) &= (U^*(x,t;j,n), E^*(x,t;j,n)). \end{aligned} \tag{11}$$

From Eq. (9), it can be seen that E is a function of U and $U_t = -E_x$. Consequently, U_t is a function of both U and U_x. In other words, the only independent discrete variables to be solved in the CESE marching scheme are $(U)_j^n$ and $(U_x)_j^n$, respectively.

Combining Eqs. (9)–(11), it can be shown that

$$\begin{aligned} (\Delta x)_j (U)_j^n = {} & \frac{(\Delta x)_{j,L}}{2}\left[(U)_{j-1/2}^{n-1/2} + \frac{(\Delta x)_{j,L}}{4}(U_x)_{j-1/2}^{n-1/2}\right] \\ & + \frac{(\Delta t)^n}{2}\left[(E)_{j-1/2}^{n-1/2} + \frac{(\Delta t)^n}{4}(E_t)_{j-1/2}^{n-1/2}\right] \\ & + \frac{(\Delta t)_{j,R}}{2}\left[(U)_{j+1/2}^{n-1/2} - \frac{(\Delta x)_{j,R}}{4}(U_x)_{j+1/2}^{n-1/2}\right] \\ & - \frac{(\Delta t)^n}{2}\left[(E)_{j+1/2}^{n-1/2} + \frac{(\Delta t)^n}{4}(E_t)_{j+1/2}^{n-1/2}\right]. \end{aligned} \tag{12}$$

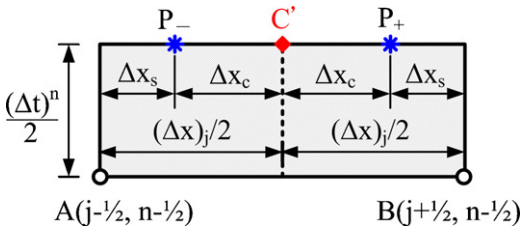

Fig. 3. Definition of points P_- and P_+ in CE when using CFL number insensitive scheme with non-uniform mesh. Note that $\Delta x_s=(1-|\Gamma|)(\Delta x)_j/4$, $\Delta x_c=(1+|\Gamma|)(\Delta x)_j/4$.

Referring to Fig. 2(b), the term on the LHS of Eq. (12) gives the flux of $\vec{h}_m$ across the upper surface of CE(j, n), while the first and second terms on the RHS of Eq. (12) represent the fluxes of $\vec{h}_m$ across the lower and left surfaces of CE(j, n), respectively, about point $(j-1/2, n-1/2)$. Finally, the third and fourth terms denote the fluxes of $\vec{h}_m$ across the lower and right surfaces of CE(j, n), respectively, about point $(j+1/2, n-1/2)$. Note that here the solved $(U)_j^n$ is located at point C' (i.e. the center of line segment AB) in Fig. 2(b).

3.2. CFL number insensitive CESE scheme

The conventional CESE scheme is a simple explicit method and provides a high-resolution performance when analyzing sharp variations in the solution domain. In implementing the CESE method, the CFL number should be assigned a value of ≤ 1 while the diffusion number (i.e. $D(\Delta t)^n/(\Delta x)_j^2$) should have a value of ≤ 0.5 in order to suppress numerical oscillations [23]. However, at very small values of the CFL and diffusion numbers, e.g. <0.01 and <0.05, respectively, the CESE scheme becomes overly dissipative. In the electrophoresis separation problems considered in the present simulations, the migration velocities of the analytes vary significantly as a result of the steep distribution of the initial electric field. Additionally moving mesh may cause large spatial intervals. Consequently, the local CFL number also varies over a large range, and may therefore result in numerical dissipation. In this study, the effects of numerical dissipation are suppressed by utilizing the CFL number insensitive CESE (CNI-CESE) scheme proposed by Chang [26].

The CNI-CESE scheme is constructed simply to solve special differential term $(U_x)_j^n$ to take account of the CFL number effect. Note that hereafter, the CFL number is denoted simply as (i.e. $\Gamma = V_e(\Delta t)^n/(\Delta x)_j$). Let P_- and P_+ be defined as the points indicated in Fig. 3. Furthermore, let $U'(P_\pm)$ be a first-order Taylor's approximation of U at point $P_\pm$ evaluated using the marching variables at $(j \pm 1/2, n-1/2)$, i.e.

$$U'(P_\pm) = (U)_{j\pm1/2}^{n-1/2} + \frac{(\Delta t)^n}{2}(U_t)_{j\pm1/2}^{n-1/2} \mp \frac{(1-|\Gamma|(\Delta x)_j)}{4}(U_x)_{j\pm1/2}^{n-1/2}. \tag{13}$$

The spatial derivatives $(\hat{U}_{x\pm})_j^n$ between (j, n) and $P_\pm$ can be defined as

$$(\hat{U}_{x\pm})_j^n = \pm\frac{U'(P_\pm) - (U)_j^n}{(1+|\Gamma|)(\Delta x)_j/4}. \tag{14}$$

Finally, the spatial differential term $(U_x)_j^n$ at point C′ can be calculated in accordance with

$$(U_x)_j^n = \frac{[1+(s_-)_j^n]^\beta(\hat{U}_x)_j^n + [1+(s_+)_j^n]^\beta(\hat{U}_{x-})_j^n}{[1+(s_-)_j^n]^\beta + [1+(s_+)_j^n]^\beta}, \tag{15}$$

where $(s_\pm)_j^n \overset{\text{def}}{=} (|(\hat{U}^+_{x\pm})_j^n|/\min(|(\hat{U}^+_{x+})_j^n|, |(\hat{U}^+_{x-})_j^n|)) - 1 \geq 0$.

Eqs. (12) and (15) yield the variables $(U)_j^n$ and $(U_x)_j^n$ at point C′. However, before repeating the solution procedure at the next time step, it is first necessary to determine the corresponding solutions at point C (see Fig. 2(b)). Solution U is linearly distributed in the SE domain due to the use of a first-order Taylor series expansion, and thus the following formulation can be derived:

$$\begin{aligned}(U)_C &= (U)_{C'} + (X_C - X_{C'})(U_x)_{C'},\\ (U_x)_C &= (U_x)_{C'}.\end{aligned} \tag{16}$$

4. Adaptive moving mesh method

The moving mesh method employed in this study was originally proposed by Tang [18], and can be summarized as follows. (a) Apply a uniform spatial grid on which the approximated solutions exist at the center points of the line segments. (b) Solve the mesh equation (see Eq. (18), below) to redistribute the grids in such a way as to increase the resolution near the critical points within the solution domain. (c) Update the approximate solutions on the new grid system using the high-resolution conservation interpolation formula (see Eq. (22), below). (d) Utilize the non-uniform CESE method in the physical domain to compute the solution to the governing equations as a function of physical time.

4.1. Adaptive mesh redistribution

In accordance with the method presented in [18], the adaptive moving mesh is generated by transforming the uniform mesh in the computational domain Ω_c to a cluster of grid points in the regions of the physical domain Ω_p characterized by solutions with large gradients. The mesh map is generated by minimizing the following function:

$$E(\eta) = \frac{1}{2}\int_{\Omega_p} \Phi^{-1}(\eta_x)^2 \mathrm{d}x, \tag{17}$$

where x and η denotes the physical and computational coordinates, respectively, Φ is called the *monitor function*. And the employed monitor function will be introduced in Section 4.3. In practice, we derive the moving mesh by solving the conventional equidistribution principle: Φx_η = constant, or $(\Phi x_\eta)_\eta = 0$ [18]. After utilizing central difference approximations we can obtain the moving mesh equation as:

$$X_j^{[\lambda+1]} = \frac{\Phi(u_{j-1/2}^{[\lambda]})X_{j-1}^{[\lambda+1]} + \Phi(u_{j+1/2}^{[\lambda]})X_{j+1}^{[\lambda]}}{\Phi(u_{j-1/2}^{[\lambda]}) + \Phi(u_{j+1/2}^{[\lambda]})}, \tag{18}$$

where $u_{j+1/2}$ represents the cell-averaged value of solution u(x) over the region $[x_j, x_{j+1}]$ and λ denotes the number of iterations. The discrete system given in (18) can be solved with the Dirichlet boundary condition using an explicit iteration method such as the Gauss–Seidel scheme.

During the solution procedure, the mesh movement is controlled using a standard gradient-based monitor function. However, in place of the conventional arc length-type monitor function, this study utilizes the more sophisticated monitor function proposed by Beckett and Mackenzie [20] in order to overcome the problem that some of the parameters used to control the monitor function are problem dependent. van Dam and Zegeling [30] showed that this particular monitor function provides an excellent tracking performance for both small, local phenomena and large shocks within the same solution domain As a result, it provides an ideal means of controlling the mesh movement in the IEF and ITP problems considered in this study. Consider a solution-dependent floor value $\psi(U)$, where $\psi(U)$ is defined as the average value of the solution gradient contained function, and the monitor function is

defined as:

$$\Phi(U) = \sum_{p=1}^{m} \left[(1-\gamma)\psi_p(U) + \gamma \left| \frac{\partial U_p}{\partial \eta} \right| \right], \quad (19)$$

where m is the number of variables, and ψ_p is derived as

$$\psi_p(U) = \int_{\Omega_c} \left| \frac{\partial U_p}{\partial \eta} \right|^{1/2} d\eta. \quad (20)$$

In theory, parameter γ in Eq. (19) can be varied by the user in accordance with solution gradients. However, in a series of preliminary investigations, it was found that a value of $\gamma = 0.8$ yielded acceptable results for a range of electrophoresis problems, and thus its value was specified as a constant $\gamma = 0.8$ in all the simulations performed in this study. (Note that a detailed investigation into the setting and effects of γ is available in [19].)

In moving mesh methods, some form of temporal or spatial smoothing is generally applied to the monitor function in order to smooth the obtained meshes, thereby avoiding the generation of highly singular meshes and suppressing large approximation errors in the regions of the solution domain characterized by large gradients. In this study, the monitor function was smoothed using the following formulation:

$$\Phi_{j+1/2}^{\text{smooth}} = \frac{1}{16}(\Phi_{j-3/2} + 3\Phi_{j-1/2} + 8\Phi_{j+1/2} + 3\Phi_{j+3/2} + \Phi_{j+5/2}). \quad (21)$$

where $\Phi_{j+1/2}$ represents $\Phi(x_{j+1/2})$.

4.2. Solution updating on new mesh

For convenience, let x_j and $\tilde{x}_j$ be the coordinates of the old mesh and the new mesh, respectively. In other words, grid point x_j in the original mesh is moved to position $\tilde{x}_j$ in the new mesh after solving the mesh equation given in (18). As a result, the solution U must be updated to reflect the change in the grid point positions. Tang [18] showed that the update procedure could be performed using the following perturbation-based conservation interpolation formula:

$$\tilde{U}_{j+1/2} = \frac{(x_{j+1} - x_j)U_{j+1/2} - [(QU)_{j+1} - (QU)_j])}{\tilde{x}_{j+1} - \tilde{x}_j}, \quad (22)$$

where $\tilde{U}$ is the solution on the new mesh, $Q(x) \equiv x - \tilde{x}$ represents a small displacement between the old and new meshes, and (QU) is the approximated numerical flux.

4.3. Adaptive time interval of CESE method

As described above, the grid points are moved to a new position in accordance with Eq. (18) and the solutions for the species concentration are then updated using Eq. (22). Simultaneously, the solutions for the conductivity σ, local electrical field, and electrophoretic velocities of the various analytes are then computed for the new mesh. Applying the constraint conditions which guarantee the stability of the CESE solver solutions (i.e. a CFL number of ≤ 1 and a diffusion number of ≤ 0.5), the time-step interval Δt for the following simulation time step is determined in accordance with

$$(\Delta t)^n = \min \left\{ \left(\frac{\Delta x}{V_{e,i}} \right)_j, \left(\frac{1}{2} \frac{\Delta x^2}{D_i} \right)_j \right\}, \quad 1 \leq j \leq N. \quad (23)$$

5. Results and discussion

This section evaluates the performance of the proposed AMR–CESE scheme when applied to the solution of three classical electrophoresis separation problems. The simulations commence by considering the ITP separation problem in which a mixture of two samples is separated under the effects of a Coulomb force and the two samples then migrate with a constant velocity. The simulations then consider the concentration of a single sample via the IEF effect induced by IPG. Finally, the simulations consider the isoelectric focusing of a sample within 10 background ampholytes. In conducting the simulations, the performance of the proposed AMR–CESE scheme is benchmarked against that of two fixed-grid solvers, namely the original CESE method and FVM. In every case, the simulations are performed on an XP-based computer (Intel I CoreI2 Duo CPU, 2.67 GHz, 2GB RAM).

5.1. Isotachophoresis (ITP) separation

In the ITP simulations, the leading electrolyte (LE) was composed of 18 mM sodium hydroxide ($\omega = 5.19 \times 10^{-9}$ m^2/Vs) and 20 mM acetic acid (pK = 4.75, $\omega = 4.24 \times 10^{-9}$ m^2/Vs), while the terminating electrolyte (TE) and background electrolyte were assumed to be 40 mM β-alanine (pK = 3.3, $\omega = 3.6 \times 10^{-8}$ m^2/Vs) and 20 mM acetic acid, respectively. Finally, the sample comprised a mixture of aniline and pyridine, and was introduced into the 4 cm long capillary channel in 1 mm long plugs with a concentration of 10 mM. The separation process was achieved by applying a current density of 2260 A/m^2 along the length of the capillary channel, resulting in the formation of a discontinuous electrical driving force on the two components within the sample. Since the different components within the sample have different mobility characteristics, they migrate at different velocities, and therefore start to separate. To avoid the disruption of electric circuit occur, the same velocity of all electrolyte were exhibited in the steady state. Fig. 4(a) presents the results obtained by the AMR–CESE scheme with 401 grids at time t = 30 min for the steady-state concentration profiles of the TE, LE, background electrolyte and sample components, respectively. The corresponding time-based variation of the time-step interval (Δt) is illustrated in Fig. 5(a), while the mesh history is presented in Fig. 5(b). The results presented in Fig. 5(b) confirm that the AMR scheme leads to a clustering of the grid points within specific regions of the solution domain. The concentration of the grid points improves the resolution of the solutions in the regions of the solution domain characterized by abrupt changes in the concentration profiles of the electrolytes or the sample components. Thus, as shown in Fig. 4(b), the results obtained using the AMR–CESE scheme with 401 grids are comparable to those obtained using the conventional CESE scheme with 2001 grids. In addition, it is observed that the conventional CESE method and the FVM method with first-order upwind scheme treating the convection term both fail to predict the concentration profiles of the two samples correctly when implemented using 401 uniform grids due to the severe numerical dissipation induced at the boundary between the samples. Fig. 6(a) compares the results obtained using the AMR–CESE scheme and other numerical schemes, respectively, for the variation of the boundary thickness between the pyridine and aniline zones as a function of the number of grid points. Note that the boundary thickness is defined here as the distance over which the concentration changes from 1% to 99% of its plateau value, both schemes show that the predicted value of the boundary thickness reduces with an increasing number of grid points. In addition, for a constant number of grid points, the boundary thickness predicted by the AMR–CESE scheme is lower than that predicted by the original CESE scheme. In other words, the AMR–CESE scheme has an improved resolution. The figure also shows Bercovici's results are superior to others, while both AMR–CESE and Sounart's solutions are comparable. Although the accuracy of Bercovici's solver is higher than AMR–CESE scheme in ITP case, this work presents further applications of the AMR–CESE to IEF problems which Bercovici's did not carry out. Finally, Fig. 6(b)

Table 1
Initial properties of acid, base and Histidine sample used in IEF IPG simulations.

Name	Concentration	Valence	p*K*	Mobility (10^{-9}), m^2/Vs
Cacodylic acid (CACO)	40 (mM) (x = 0 cm) ~ 20 (mM) (x = 1 cm), linear distribution	−1	6.184	0
Tris-aminomethane (TRIS)	20 (mM) (x = 0 cm) ~ 40 (mM) (x = 1 cm), linear distribution	+1	8.076	0
Histidine (HIS)	1 (mM) uniform distribution (t = 0 s)	−1	9.17	20.2
		+1	6.04	20.2

compares the consumed CPU times of the AMR–CESE and CESE schemes in solving the ITP problem as a function of the number of grid points. In general, the results show that for a given number of grid points, the CPU time of the AMR–CESE scheme is around twice that of the conventional CESE scheme due to the requirement to adjust the mesh adaptively during the solution procedure. However, as shown in Fig. 4(b), the AMR–CESE scheme provides the ability to obtain high-resolution insights into the ITP problem with a significantly lower number of grid points than that required by the CESE scheme. Thus, in practice, the CPU time of the AMR–CESE scheme is actually lower than that of the CESE method for an equivalent resolution.

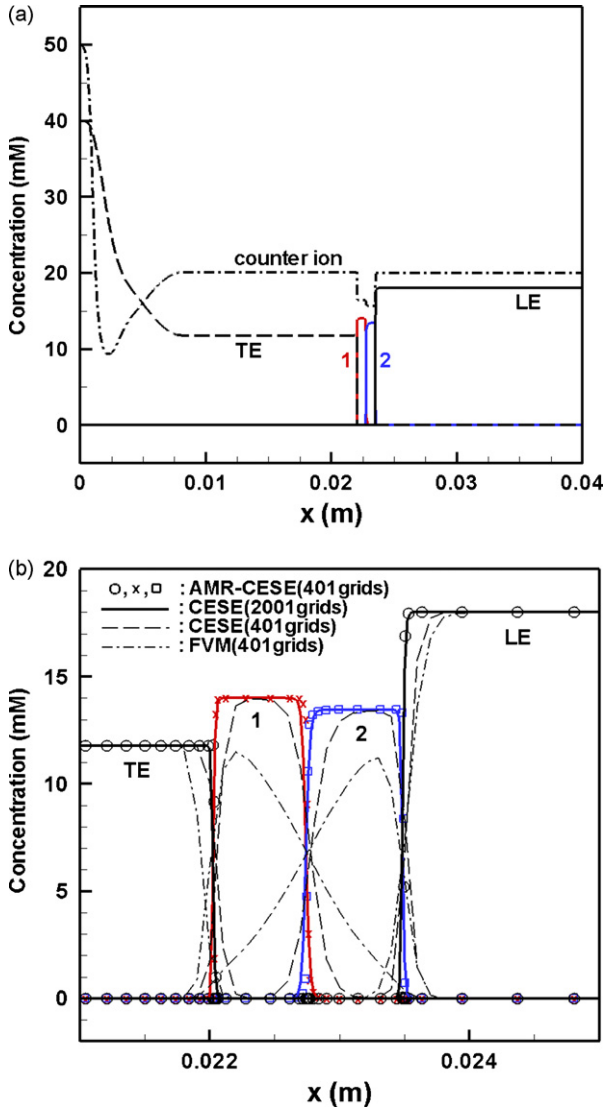

Fig. 4. Simulation results for ITP problem: (a) concentration distribution of all analytes at t = 30 min with 401 grids; (b) comparison of AMR–CESE solution with those of existing numerical methods. Note that the solid line indicates the solutions obtained using the original CESE method with a fine grid resolution (2001 grids).

5.2. Isoelectric focusing (IEF) by IPG

The second set of simulations considered the isoelectric focusing of an ampholyte sample within a straight channel of length 1 cm under the effects of an immobilized pH gradient. The simulations considered Histidine as the sample and created an immobilized pH gradient by carefully controlling the distribution of the buffer constituents, namely Cacodylic acid (CACO) and Tris-aminomethane (TRIS). In order to maintain an immobilized pH gradient, the mobilities of the buffer constituents were specified as zero and an assumption was made that the IEF process took place in the absence of a bulk flow. Table 1 summarizes the initial conditions considered in the simulations. As shown, the CACO and TRIS were linearly distributed along the length of the channel, while the Histidine sample (1 mM) was uniformly distributed. In each simulation, a current

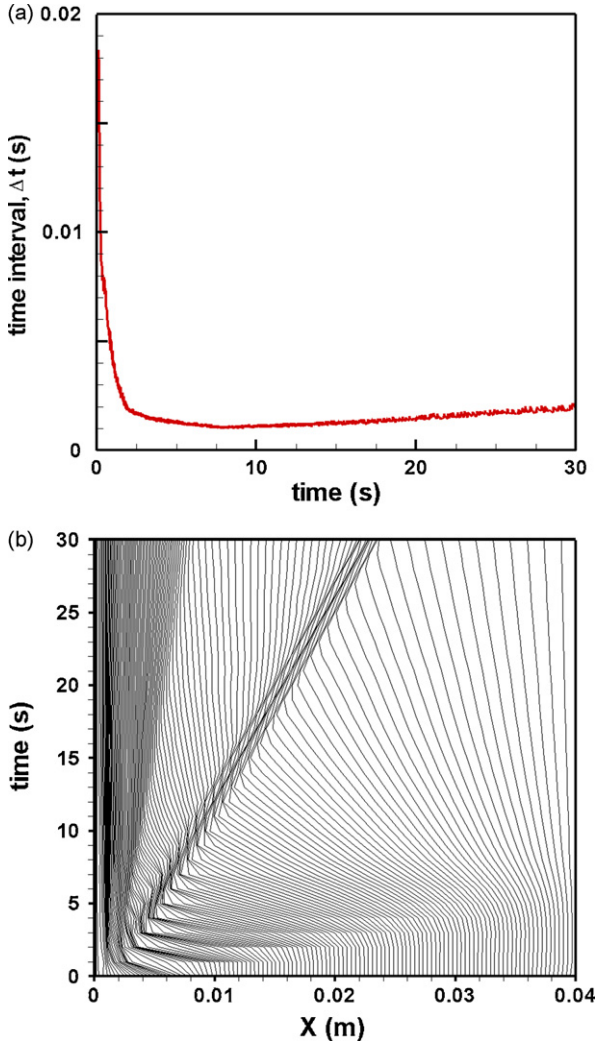

Fig. 5. Time-step and mesh variation in ITP simulation utilizing AMR–CESE scheme with 401 grids: (a) variation of selected time-step interval (Δt) over time and (b) mesh history.

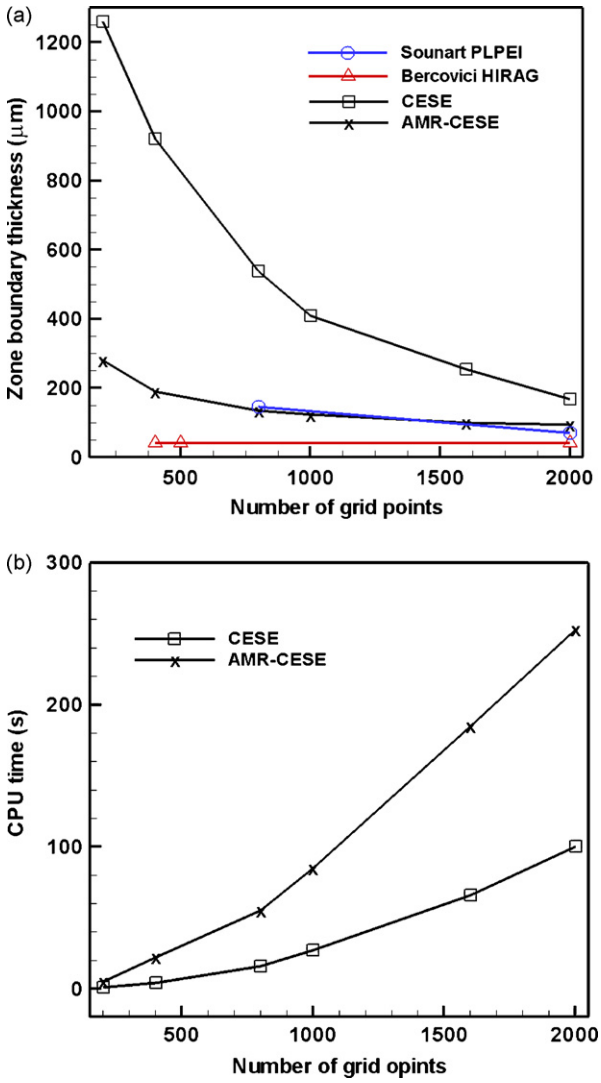

Fig. 6. Comparison of AMR–CESE results and original CESE results for ITP simulation: (a) variation of predicted boundary thickness between pyridine and aniline zones for various relevant numerical schemes as function of number of grids and (b) variation of consumed CPU time to achieve solution at $t = 30$ min as function of number of grids.

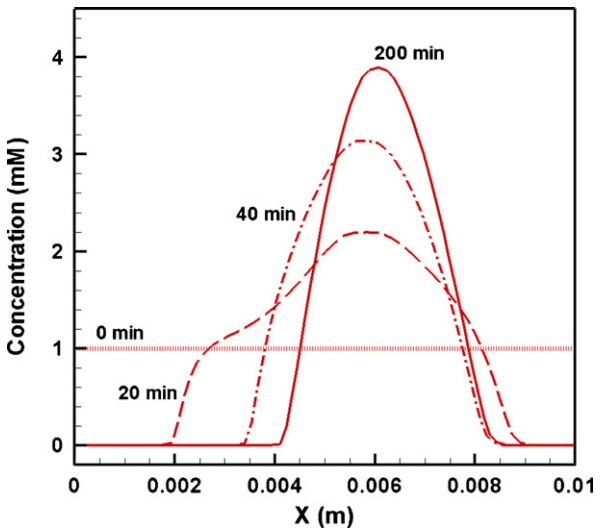

Fig. 7. Concentration evolution of Histidine in IEF IPG problem when solved by AMR–CESE scheme with 51 grids.

density of 0.2 A/m^2 was applied along the length of the channel, causing the sample to move gradually toward its p*I* location (i.e. the point of zero net Coulomb force).

Fig. 7 presents the time-based variation of the Histidine concentration profile for the case in which the IEF in IPG problem was solved by the AMR–CESE scheme with 51 grids (i.e. an initial grid size $\Delta x = 0.02$ cm).It can be observed that the shape of concentration profile is maintained since the balance between diffusion effect and the Coulomb force at about 200 min. Fig. 8(b) shows the variation of the time-step interval (Δt) over time when solving the IEF IPG problem utilizing the AMR–CESE scheme with 51 grids. Meanwhile, Fig. 8(a) illustrates the corresponding mesh history. As the Histidine sample approaches the p*I* location and attains steady-state conditions, its migration velocity reduces to zero. Thus, the time-step interval Δt reduces to a constant value of approximately 2.22 (s) (see Fig. 8(a)), and the mesh positions are no longer adjusted (see Fig. 8(b)). Fig. 9(a) and (b) compares the results obtained by the AMR–CESE scheme, the original CESE method and the FVM methods, respectively, for the concentration and conductivity profiles within the channel after $t = 200$ min. It can be seen that in both figures, the resolution of the results obtained using the AMR–CESE

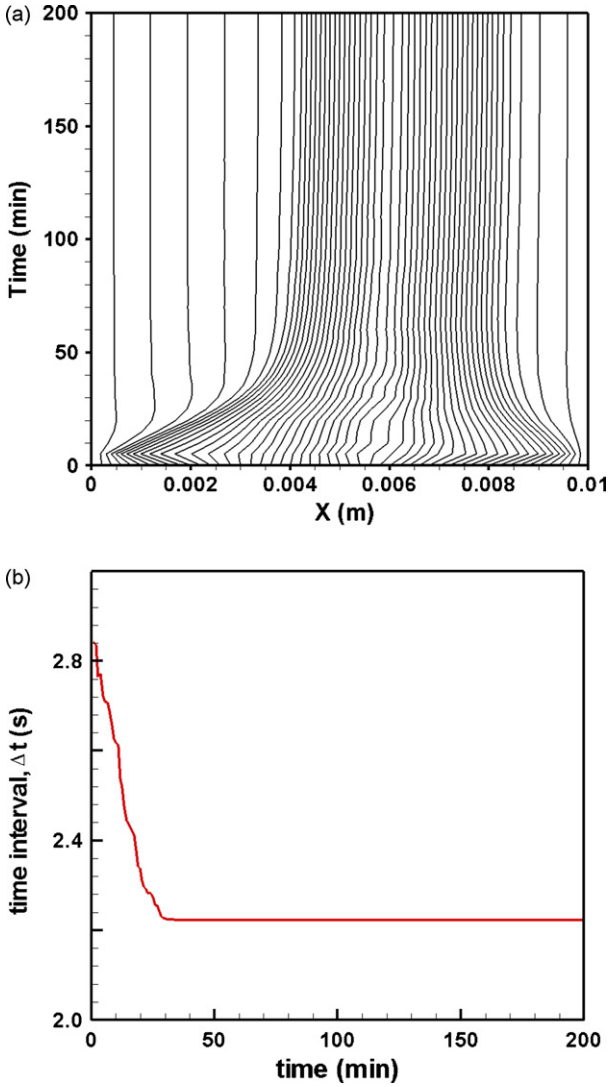

Fig. 8. Time-step and mesh variation in IEF IPG simulation when using AMR–CESE scheme with 51 grids: (a) mesh history and (b) variation of time-step interval (Δt) over time.

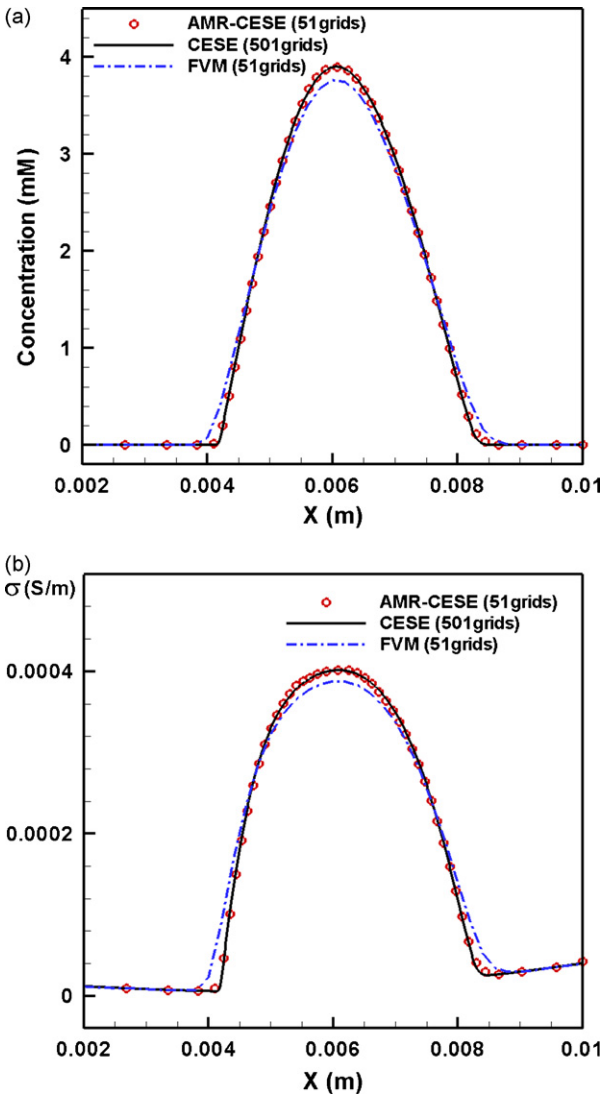

Fig. 9. Comparison of AMR–CESE solutions for IEF IPG problem at $t = 200$ min with CESE and FVM solutions: (a) Histidine concentration and (b) conductivity (σ).

method with 51 grids is equivalent to that of the solutions obtained from the conventional CESE method with 510 grids. By contrast, the results obtained using the FVM method with 51 uniform grids show clear evidence of numerical dissipation.

The accuracy of the concentration results obtained by the various simulation methods can be quantified using the following discrete L1-norm error:

$$\text{L1-norm error}(N) = \frac{1}{N}\sum_{i=1}^{N}|C_i - C_{f,i}| \tag{24}$$

where N is the total number of mesh grids in the computational domain and $|C_i - C_{f,i}|$ is the difference in the sample concentration values obtained at position x_i when using a coarse mesh and a fine mesh, respectively. Fig. 10 shows the L1-norm errors of the AMR–CESE and FVM solutions for the Histidine concentration at times $t = 20$, $t = 40$ and $t = 200$ min, respectively. Note that $N = 51$ in every case. The results show that the error of the AMR–CESE solutions is less than one half that of the FVM solutions at each considered time point. In other words, the accuracy of the AMR–CESE method is confirmed.

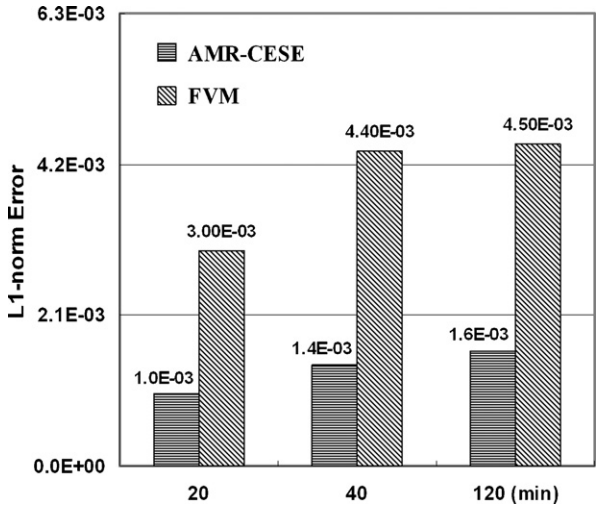

Fig. 10. Comparison of L1-norm errors of AMR–CESE and FVM schemes with 51 grids when solving IEF IPG problem.

5.3. Isoelectric focusing (IEF) of sample within 10 background ampholytes

The final set of simulations considered the focusing of a single ampholyte sample in an ampholyte-based pH gradient produced by 10 components. The properties of the 10 ampholytes and the single sample are summarized in Table 2 and are consistent with those considered in [15]. The simulations assumed the IEF process to take place within a planar channel of length 1 cm under the effects of an external electric field with an intensity of 300 V/cm. The initial grid interval within the AMR–CESE scheme was specified as $\Delta x = 5 \times 10^{-2}$ cm, giving a total of 201 grids.

As shown in Fig. 11, the sample is concentrated within a single focused band located at $x = 0.5$ cm (i.e. the midpoint position of the channel) after 30 s. From inspection, the concentration of the focused protein sample (1.5 mM) is found to be around 90 times higher than the initial concentration (i.e. ~0.16 mM, see Table 2). Fig. 12(a) and (b) illustrates the evolution of the time-step interval Δt and the adaptive mesh over time, respectively. Fig. 12(a) confirms that the time-step interval converges to a constant value under steady-state conditions. Moreover, Fig. 12(b) shows that the mesh points are clustered in the vicinity of the interfaces between the adjacent ampholytes within the channel and finally the mesh structure does not change substantially. In other words, the results confirm the ability of the AMR–CESE scheme to drive the mesh points toward the regions of discontinuity in the solution domain. Fig. 13(a) compares the sample concentration profile obtained by the AMR–CESE method with 201 grids with the profiles obtained

Table 2
Properties of 10 ampholytes and 1 sample.

Analyte	pK_1	pK_2	pI	Concentration, mol/m^3	Mobility m^2/Vs
Ampholyte 1	6.01	6.41	6.21	0.16	3.0E−8
Ampholyte 2	6.25	6.65	6.45	0.16	3.0E−8
Ampholyte 3	6.47	6.87	6.67	0.16	3.0E−8
Ampholyte 4	6.71	7.11	6.91	0.16	3.0E−8
Ampholyte 5	6.94	7.34	7.14	0.16	3.0E−8
Ampholyte 6	7.17	7.57	7.37	0.16	3.0E−8
Ampholyte 7	7.51	7.91	7.71	0.16	3.0E−8
Ampholyte 8	7.64	8.04	7.84	0.16	3.0E−8
Ampholyte 9	7.87	8.27	8.07	0.16	3.0E−8
Ampholyte 10	8.10	8.50	8.30	0.16	3.0E−8
Sample	7.00	7.60	7.30	0.16	3.0E−8

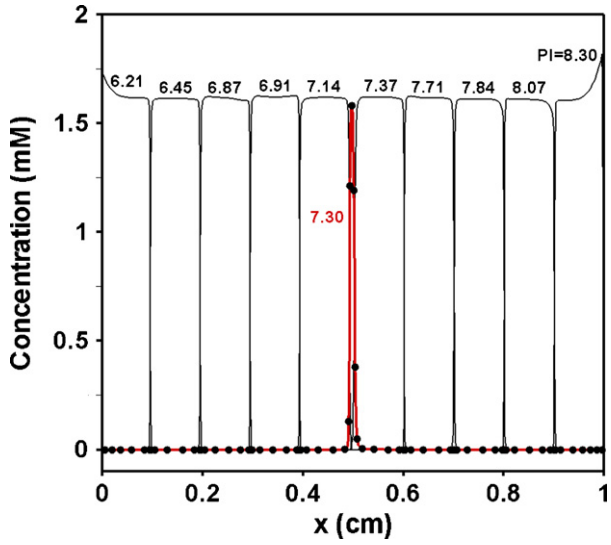

Fig. 11. Concentration profiles of sample and 10 ampholytes after $t = 30$ s in IEF problem solved using AMR–CESE scheme.

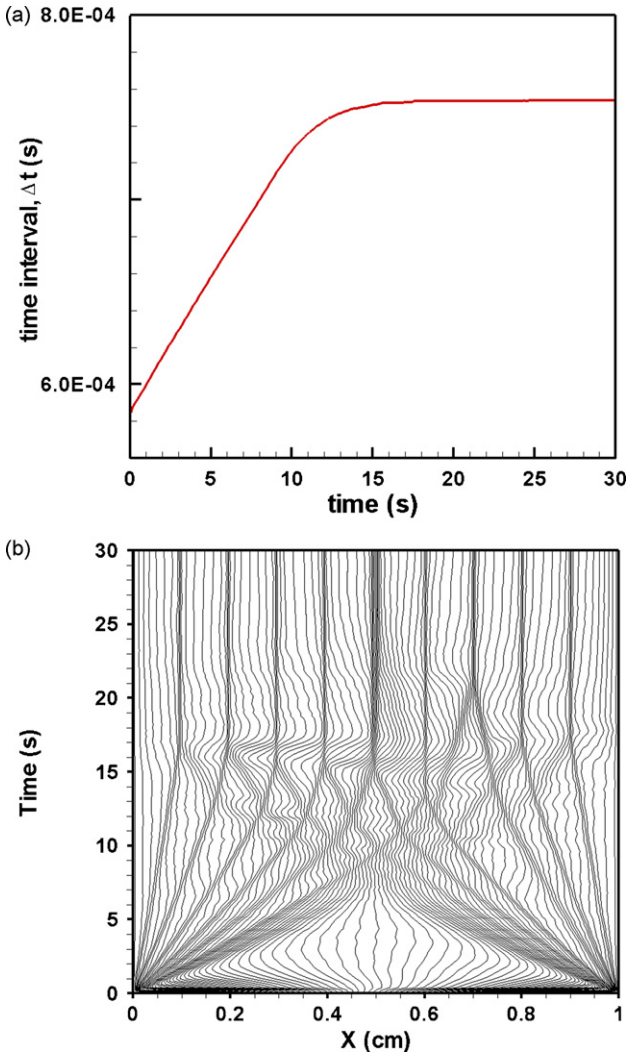

Fig. 12. Time-step and mesh variation in IEF simulation for sample and 10 background ampholytes using AMR–CESE scheme with 201 grids: (a) variation of time-step interval (Δt) over time and (b) mesh history.

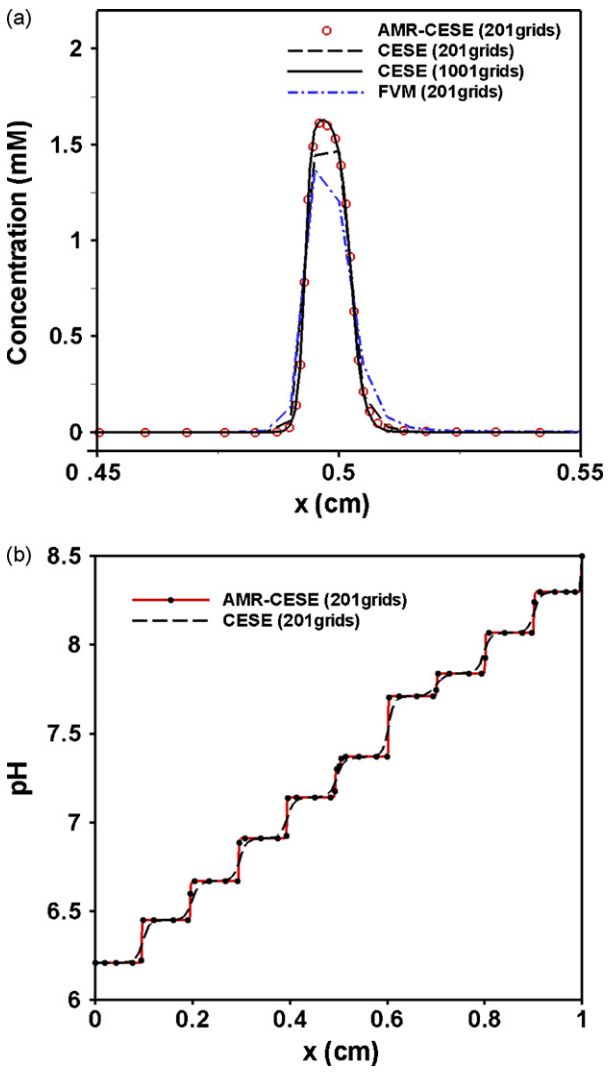

Fig. 13. Comparison of AMR–CESE solutions at $t = 30$ s for IEF problem with sample and 10 background ampholytes with solutions obtained from original CESE method and FVM method: (a) sample concentration and (b) pH profile.

by the conventional CESE method with 201 and 1001 grids, respectively, and the FVM method with 201 grids. It is observed that the resolution of the results obtained using the AMR–CESE method with a coarse mesh of 201 grids is equivalent to that obtained using the conventional CESE scheme with a fine mesh of 1001 grids. However, the results obtained from the CESE and FVM methods with a coarse mesh of 201 grids show evidence of numerical dissipation. Fig. 13(b) compares the results obtained from the AMR–CESE scheme and the conventional CESE scheme for the step-like distribution of the pH along the channel length under steady-state conditions. Note that both schemes are implemented using a coarse mesh of 201 grids. Comparing the two profiles, it is seen that the AMR–CESE method more accurately captures the points of discontinuity between the adjacent ampholytes. In other words, the AMR–CESE profile has a well-defined step-like characteristic, whereas the CESE method tends to smooth the pH boundary between the adjacent ampholytes. Finally, Fig. 14 compares the L1-errors of the concentration results obtained by the AMR–CESE scheme, the conventional CESE method and the FVM method at times of $t = 10$ s and $t = 30$ s, respectively. Note that in every case the schemes are implemented using a mesh with 201 grids. The results once again demonstrate the superior accuracy of the AMR–CESE scheme.

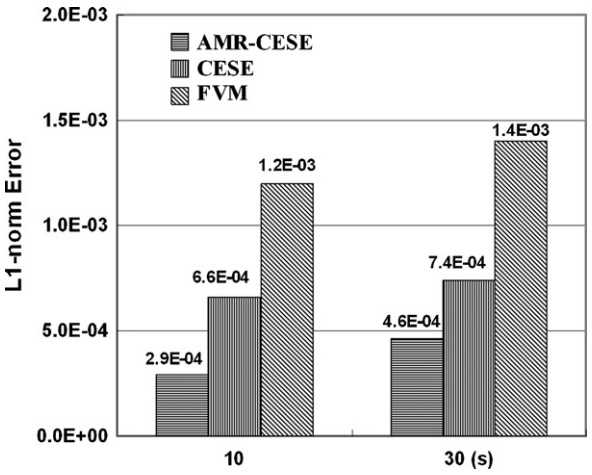

Fig. 14. Comparison of L1-norm errors of AMR–CESE scheme, original CESE method and FVM method when solving IEF problem with sample and 10 background ampholytes. Note that in each case, the schemes are implemented using a mesh with 201 grids.

6. Concluding remarks

This paper has proposed an adaptive mesh redistribution CESE (AMR–CESE) scheme based upon a moving mesh technique and the non-uniform mesh CESE method for the solution of general electrophoresis separation problems. To overcome the numerical dissipation problem induced by the very low CFL numbers caused by large local values of Δx in the non-uniform mesh, the spatial term in the CESE scheme has been treated using a CFL number insensitive method. The validity of the proposed AMR–CESE scheme has been confirmed by solving several classical electrophoresis separation problems, namely isotachophoresis (ITP), isoelectric focusing (IEF) in an immobilized pH gradient (IPG), and IEF of a sample within 10 background ampholytes. The results have shown that the AMR–CESE scheme successfully resolves the points of discontinuity in the concentration distributions in the ITP and ampholyte-based pH gradient IEF problems. In addition, for a given resolution, the proposed method yields a significant reduction in the number of grid points compared to uniform mesh methods. Overall, the results show that the AMR–CESE scheme is an ideal numerical solver for problems in which the solutions are highly singular within fairly localized regions.

Acknowledgement

The authors gratefully acknowledge the financial support provided to this study by the Nation Science Council of Taiwan under Project Nos. NSC97-2221-E-006-136-MY3 and NSC98-2811-E006-028. We are also grateful to the National Center for High-performance Computing for sparing computer time and providing facilities.

References

[1] P.G. Righetti, J. Chromatogr. A 1079 (2005) 24.
[2] P. Gebauer, Z. Malá, P. Boček, Electrophoresis 28 (2007) 26.
[3] L. Křivánková, P. Pantůčková, P. Boček, J. Chromatogr. A 838 (1999) 55.
[4] S.H. Shim, A. Riaz, K.W. Choi, D.S. Chung, Electrophoresis 24 (2003) 1603.
[5] H. Cui, P. Dutta, C.F. Ivory, Electrophoresis 28 (2007) 1138.
[6] V. Hruška, M. Jaroš, B. Gaš, Electrophoresis 27 (2006) 984.
[7] W. Thormann, R.A. Mosher, Electrophoresis 27 (2006) 968.
[8] J.W. Yu, Y. Chou, R.J. Yang, Electrophoresis 29 (2008) 1048.
[9] M. Bercovici, S.K. Lele, J.G. Santiago, J. Chromatogr. A 1216 (2009) 1008.
[10] L.H.H. Silvertand, J.S. Torano, W.P. van Bennekom, G.J. de Jong, J. Chromatogr. A 1204 (2008) 157.
[11] R.A. Mosher, W. Thormann, M. Bier, J. Chromatogr. 351 (1986) 31.
[12] R.A. Mosher, W. Thormann, Electrophoresis 11 (1990) 717.
[13] T.L. Sounart, J.C. Baygents, J. Chromatogr. A 890 (2000) 321.
[14] A. Chatterjee, J. Micromech. Microeng. 13 (2003) 758.
[15] J. Shim, P. Dutta, C.F. Ivory, Electrophoresis 28 (2007) 572.
[16] Y. Chou, R.J. Yang, Electrophoresis 30 (2009) 819.
[17] W. Thormann, J. Caslavska, M.C. Breadmore, R.A. Mosher, Electrophoresis 30 (2009) S16.
[18] H.Z. Tang, T. Tang, SIM J. Numer. Anal. 41 (2003) 487.
[19] W. Huang, J. Comput. Phys. 171 (2001) 753.
[20] G. Beckett, J.A. Mackenzie, Appl. Numer. Math. 35 (2000) 87.
[21] C. Jin, K. Xu, J. Comput. Phys. 218 (2006) 68.
[22] H.Z. Tang, Int. J. Numer. Meth. Fluids 44 (2004) 789.
[23] S.C. Chang, J. Comput. Phys. 119 (1995) 295.
[24] T.I. Tseng, R.J. Yang, AIAA J. 44 (2006) 1040.
[25] Y. Chou, R.J. Yang, Int. J. Heat Mass Transfer 51 (2008) 3525.
[26] S.C. Chang, AIAA Paper 2002–3890 (2002).
[27] D.A. Saville, O.A. Palusinski, AIChE J. 32 (1986) 207.
[28] H. Cui, K. Horiuchi, P. Dutta, C.F. Ivory, Anal. Chem. 77 (2005) 1303.
[29] H. Cui, K. Horiuchi, P. Dutta, C.F. Ivory, Anal. Chem. 77 (2005) 7878.
[30] A. van Dam, P.A. Zegeling, J. Comput. Phys. 216 (2006) 526.